Surface photovoltage spectroscopy as a valuable nondestructive characterization technique for GaAs/GaAlAs vertical-cavity surface-emitting laser structures

2003 J. Phys.: Condens. Matter 15 55

(http://iopscience.iop.org/0953-8984/15/2/306)

INSTITUTE OF PHYSICS PUBLISHING JOURNAL OF PHYSICS: CONDENSED MATTER

J. Phys.: Condens. Matter **15** (2003) 55–66 PII: S0953-8984(03)52383-9

Surface photovoltage spectroscopy as a valuable nondestructive characterization technique for GaAs/GaAlAs vertical-cavity surface-emitting laser structures

J S Liang[1], S D Wang[1], Y S Huang[1,5], C W Tien[2], Y M Chang[2], C W Chen[2], N Y Li[2], K K Tiong[3] and F H Pollak[4]

[1] Department of Electronic Engineering, National Taiwan University of Science and Technology, Taipei 106, Taiwan
[2] Kingmax Optoelectronics incorporated, Hu Kou, Hsin Chu 303, Taiwan
[3] Department of Electrical Engineering, National Taiwan Ocean University, Keelung 202, Taiwan
[4] Department of Physics and New York State Center for Advanced Technology in Ultrafast Photonic Materials and Applications, Brooklyn College of the City University of New York, Brooklyn, NY 11210, USA

Received 8 August 2002
Published 20 December 2002
Online at stacks.iop.org/JPhysCM/15/55

Abstract

We have investigated an 850 nm GaAs/GaAlAs (001) vertical-cavity surface-emitting laser (VCSEL) structure using angle- and temperature-dependent surface photovoltage spectroscopy (SPS). The SPS measurements were performed as functions of angle of incidence ($0° \leqslant \theta \leqslant 60°$) and temperature ($25\,°C \leqslant T \leqslant 215\,°C$) for both the metal–insulator–semiconductor (MIS) and wavelength-modulated MIS configurations. Angle-dependent reflectance (R) measurements have also been performed to illustrate the superior features of the SPS technique. The SPS spectra exhibit both the fundamental conduction to heavy-hole excitonic transition of quantum well and cavity mode (CM) plus a rich interference pattern related to the mirror stacks, whereas in the R spectra only the CM and interference features are clearly visible. The variations of SPS spectra as functions of incident angle and temperature enable exploration of light emission from the quantum well confined in a microcavity with relation to the Fabry–Pérot cavity mode. The results demonstrate considerable potential of SPS for the contactless and nondestructive characterization of VCSEL structures.

[5] Author to whom any correspondence should be addressed.

1. Introduction

Vertical-cavity surface-emitting lasers (VCSELs) have optical cavities orthogonal to the conventional edge-emitting diode lasers and serve as important radiation sources for many applications, such as local area communication, optical data storage, optical bus system and optical computing [1, 2]. Compared to the edge-emitting laser, VCSELs have a number of advantages including single-longitudinal-mode operation, symmetric-beam profile, small beam divergence, low threshold current and ease of integrability and testability [2–4]. The basic structure of a VCSEL is a Fabry–Pérot (FP) cavity consisting of an active region with embedded quantum wells (QWs), sandwiched between two multilayer distributed Bragg reflector (DBR) stacks that form highly reflecting mirrors with a broad reflectance stop band centred on a certain free space wavelength, λ_{Bragg}. Generally, both DBR stacks are highly p(upper)/n(lower) doped, so that the whole structure forms a p–i–n diode. The overall optical thickness of the active region determines the approximate cavity length, which is usually a few integer multiples of half of the intended lasing wavelength. The interaction between the DBRs and cavity produces a sharp FP dip in the R spectrum at the cavity wavelength λ_{cav}, usually positioned at the centre of the stop band. The fundamental conduction to heavy-hole (1C–1H) excitonic transition, which occurs at a wavelength of λ_{QW}, provides the gain. To achieve the desired performance, VCSELs are designed such that λ_{QW} coincides with λ_{cav} at operation temperature. This means that λ_{QW} at room temperature must be chosen to be shorter than λ_{cav} so that local temperature increase during operation may compensate for the offset. In order to reduce production costs and to assure reproducibility, better means of growth and characterization need to be developed. Therefore, a contactless and nondestructive method to rapidly determine the excitonic transition of the QWs, the cavity mode (CM) and the thickness of the quarter-wavelength layers in the DBRs of an epitaxial structure before laser processing is of importance to the manufacturer.

The nondestructive characterization of VCSELs presents a considerable challenge since photoluminescence [5], a technique that has been employed to characterize edge-emitting lasers, is not very useful for VCSELs because of the high DBR reflectivity. The reflectivity (R) [7–13] of a VCSEL is determined by the physical structure of the DBRs and cavity. Reflectivity measurements yield λ_{cav}, but generally provide no information about λ_{QW}. Hence the R spectrum is not useful for checking the degree of mismatch between the two wavelengths. Other useful optical diagnostic techniques such as contactless electroreflectance (CER) [6] and photoreflectance (PR) [7–14] yield, at room temperature, signals that make it possible to evaluate λ_{QW}, and in some cases λ_{cav} as well as the built-in electric field in the i-region from the Franz–Keldysh oscillations. Jaeger *et al* [15] have also reported room temperature angle-dependent photocurrent spectroscopy that yields λ_{QW} and λ_{cav}. More recently, Huang *et al* [16], Liang *et al* [17, 18] and Huang *et al* [19] have reported surface photovoltage spectroscopy (SPS) to characterize the 980 nm InGaAs/GaAs/GaAlAs, 850 nm GaAs/GaAlAs and 1.3 μm InGaAlAs/InP VCSELs. So far, the SPS technique offers many superior features over the other methods of characterization and deserves further exploration.

In the SPS spectra of VCSELs, features of the ground state QW transition and the CM can be detected simultaneously. If the signals from both features are too close to be resolved, one can increase the angle of incidence θ of the probe light to shift λ_{cav} to shorter wavelengths while leaving λ_{QW} unchanged. This works well as, for most practical cases we have encountered, $\lambda_{cav}(\theta = 0^\circ)$ and λ_{QW} are usually quite close to each other at room temperature. An alternative approach may also be implemented through an increase of the sample temperature T at fixed incident angle θ. This will shift λ_{QW} to the longer wavelength region while λ_{cav} will also increase but at a slower pace.

In this paper, we present detailed angle- and temperature-dependent SPS and R studies on an 850 nm GaAs/GaAlAs VCSEL structure. For the SPS measurements, both the conventional metal–insulator–semiconductor (MIS) and wavelength modulated MIS configurations were performed as functions of incident angle ($0° \leqslant \theta \leqslant 60°$) and temperature (25 °C $\leqslant T \leqslant$ 215 °C). The SPS spectra displayed λ_{QW} and λ_{cav} as well as a rich interference pattern from the DBRs. The wavelength modulation MIS configuration yields a derivative-like surface photovoltage (DSPV) spectrum. By analysing the DSPV spectra through an appropriate line shape fit, the wavelengths of both λ_{QW} and λ_{cav} may be determined accurately. The results indicate that SPS is a powerful tool for a completely contactless and nondestructive characterization of wafer-scale VCSEL structures.

2. Experimental details

In this study we have used a typical top-emitting VCSEL unprocessed structure using the GaAs/GaAlAs-based material system. The VCSEL was grown by metallorganic chemical vapour deposition (MOCVD) on an n^+-GaAs(001) substrate, and consisted of an active QW gain region embedded between two DBRs. The mirrors consist of a 30-period $Ga_{0.08}Al_{0.92}As/Ga_{0.88}Al_{0.12}As$ n-doped high-reflectivity DBR and a 19-period $Ga_{0.08}Al_{0.92}As/Ga_{0.88}Al_{0.12}As$ p-doped output DBR. The active region contained three undoped 60 Å GaAs wells and 80 Å $Ga_{0.7}Al_{0.3}As$ barriers, centred in $Ga_{0.7}Al_{0.3}As/Ga_{1-x}Al_xAs$ ($x = 0.3$–0.6) spacer layers to form a single-wavelength cavity. $Ga_{0.02}Al_{0.98}As$ with a thickness of 613 Å layers were placed in the VCSEL structure above and below the active region for selective lateral oxidation to provide optical and electrical confinement. The emission wavelength for the fabricated VCSEL devices is in the range of 845–855 nm. The threshold current is about 0.2–0.4 mA with an aperture size from 4.2 to 6.2 μm in the devices.

SPS is based on the measurement of the change of photovoltaic response of semiconductors as a function of the wavelength of the incident illumination [20–23]. In this study both the conventional MIS and wavelength modulated MIS configurations were used. In the conventional MIS configuration, the contact potential difference between the sample and a reference grid electrode is measured in a capacitive manner as a function of the wavelength of the probe beam by holding the grid fixed and chopping the probe beam at 193 Hz. The light from a 150 W quartz–halogen lamp was passed through a 0.2 m grating monochromator and projected onto the sample. The incident light intensity was maintained at a constant level of 10^{-4} W cm^{-2} by using a mechanical servo with a variable neutral density filter. A beam splitter was placed in the path of the incident light. The intensity of this radiation was monitored by a power meter and was kept constant by a stepping motor connected to a variable neutral density filter, which was also placed in the path of the incident beam. Since our measurements were performed over a rather narrow photon energy range, constant intensity is essentially equivalent to constant photon flux. The induced surface photovoltage (SPV) on the metal grid was measured with a metal bottom as the ground electrode, using a buffer circuit and a lock-in amplifier. For the wavelength modulated MIS configuration, the DSPV spectrum was obtained. The illumination system consisted of a 150 W quartz–halogen lamp and a grating monochromator equipped with a vibrating exit slit. The illumination intensity and the amplitude of wavelength modulation were experimentally selected at levels not affecting the measured spectra; typically $\Delta\lambda/\lambda_0$ was of the order of 10^{-3}. Precautions were taken to eliminate the spurious signal from light-intensity modulation. The method of reflectance has been described in the literature [7–13].

3. Theoretical background

3.1. Angle dependence of SPS and R

To a first approximation, a VCSEL structure consisting of two DBRs and a cavity can be considered as an etalon of effective thickness d and mean refractive index n. The CM dip feature in the R spectrum occurs at a wavelength λ_{cav} given by the condition that the rays reflected at the front and back surfaces of the etalon interfere destructively. Taking the π phase change at the back surface into account, a simple dependence of λ_{cav} on external angle of incidence θ in our SPS and R measurements can be expressed as [8]

$$\lambda_{cav}(\theta) = \frac{2nd}{m}\sqrt{1 - \frac{\sin^2\theta}{n^2}} = \lambda_{cav}(0^\circ)\sqrt{1 - \frac{\sin^2\theta}{n^2}} \tag{1}$$

where $m = 1, 2, 3, \ldots$, and $\lambda_{cav}(0^\circ)$ is the CM wavelength at normal incidence.

3.2. Temperature dependence of SPS

As already noted, in situations where a feature due to the QW ground state transition is not directly observable in the SPS, there are two indirect methods of acquiring information on λ_{QW} at room temperature. One way of achieving this is through a faster temperature rate of change of λ_{QW} than λ_{cav} at some fixed incident angle. Hence, they will cross at certain temperature at the onset of QW/CM resonance, giving a single estimate of $\lambda_{QW} = \lambda_{cav}$ at this temperature. Such a temperature-tuning procedure can be done for several incident angles, which will give λ_{QW} as a function of temperature. The temperature dependence of the fundamental transition energy of the QW structure, $E_{QW}(T)$, can be expressed by a Bose–Einstein-type expression [16, 19]:

$$E_{QW}(T) = E_{QW}(0) - \frac{2a_b}{[\exp(\theta_b/T) - 1]} \tag{2}$$

where $E_{QW}(0)$ is the energy at $T = 0$ K, a_b represents the strength of the average electron phonon interaction and θ_b corresponds to the average phonon temperature. For small temperature variations near and above room temperature, the behaviour of $E_{QW}(T)$ as given by equation (2) is virtually linear with temperature T. Hence, the associated wavelength λ_{QW} can be expressed as a linear function of temperature as

$$\lambda_{QW}(T) \approx \lambda_{QW}(T_r) + \alpha_{QW}(T - T_r) \tag{3}$$

where $\lambda_{QW}(T_r)$ is the wavelength at room temperature $T_r = 25\,^\circ$C, α_{QW} is a constant relating to a_b and θ_b and T is in °C. The slower variation of λ_{cav} with T over the same temperature range can also be similarly expressed except that the coefficient α_{cav} may well relate to the thermal expansion coefficient of the cavity and index of refraction n.

4. Experimental results and discussion

4.1. Room temperature near normal incident R and SPS

Figure 1(a) shows the near normal incident reflectivity (NIR) spectrum in the range of 653–953 nm. Figures 1(b) and (c) are the normal incident SPV spectrum and the numerical computed normalized first derivative of the SPV signal with respect to the wavelength $(\Delta V/\Delta\lambda)/V$, respectively, while figure 1(d) is the DSPV spectrum measured with a wavelength modulation technique. The feature that lies at the centre of the stop band at 845.8 ± 1.2 nm is the CM structure, which appeared as a dip in the NIR trace and a peak in the SPS. The features at shorter

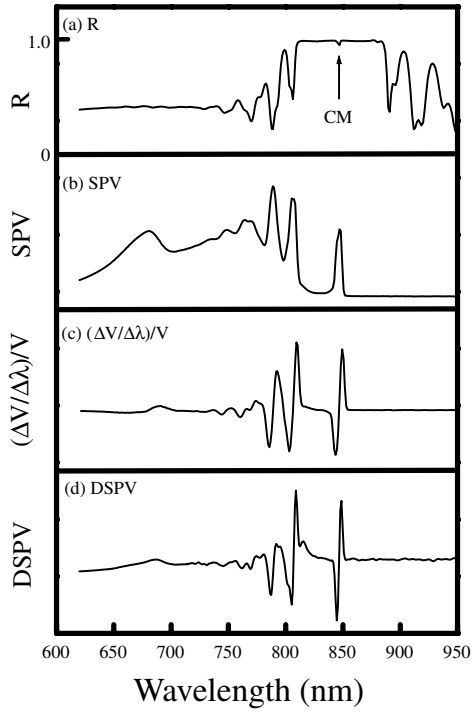

Figure 1. (a) The near normal-incident reflectivity spectrum, (b) the normal-incident SPV spectrum, (c) the numerical computed normalized first derivative of the SPV signal with respect to the wavelength and (d) the wavelength modulated DSPV spectrum. The arrow indicates the wavelength position of the CM, λ_{cav}.

wavelengths (and longer wavelengths for NIR) are due to interference from the DBRs. Note that the SPS peaks correspond to the NIR dips. In addition a broad feature around 685 nm, which originated from the GaAlAs barriers, is observed in both SPV and DSPV spectra. Careful comparison of the figures 1(c) and (d) shows that the DSPV spectrum duplicates the structural form of the numerical derivative SPV signal. The result gives convincing evidence that wavelength-modulated SPV of VCSEL structures yields a first order wavelength derivative spectrum.

4.2. Experiments at room temperature and increasing angle of incidence

Figure 2 presents room temperature SPV spectra for different θ of the probe light. The spectra clearly show several prominent features. A steplike increase of the photovoltage is detected at about 845 nm. This steplike increase corresponds to the onset of absorption of 1C–1H transitions in the GaAs QW. The second signal, which corresponds to the CM, is seen to move to shorter wavelength with increasing angle of incidence, from about 845 nm at 0° to 820 nm at 60°. The dotted line, a guide to the eye, shows the angle dependence of the CM. The structures below about 800 nm are interference effects from the DBRs.

Figure 3 displays a set of DSPV spectra measured under different incident angles θ of the light beam. In term of the dependence to the incident angle θ, the observed features can be grouped into two types. Type-I features correspond to those that shift toward shorter wavelength with increasing θ. These include the CM (dotted line) and the DBR mirror features. Type-II

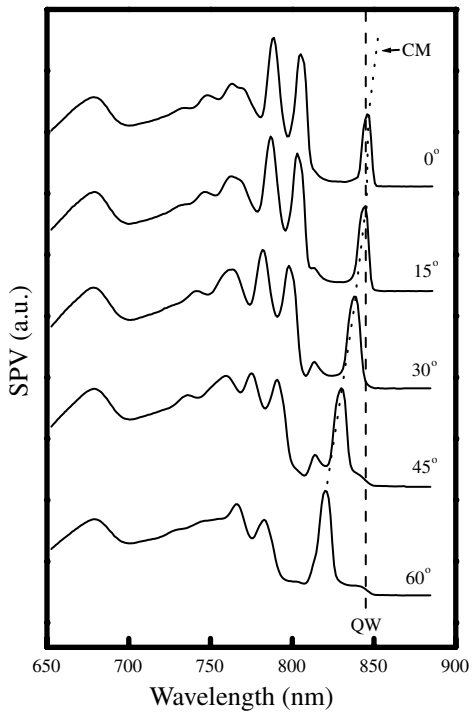

Figure 2. Room temperature SPV spectra of the VCSEL structure for different angles of incidence of the probe light. The base lines of the spectra are offset vertically for clarity. A steplike increase of the photovoltage located at ∼845 nm corresponds to the onset of absorption of 1C–1H transition in the GaAs QW. The QW transition wavelength λ_{QW} is indicated by a dashed line, and the dotted line, a guide to the eye, indicates the CM moving toward shorter wavelength with increasing angle of incidence.

features show no shift at all with the incident angle. The angle-independent type-II DSPV features are also highlighted as letters A, B and C, respectively. In figure 3 the broad feature A is observed at shorter wavelength and indicated by an arrow. An inset in the wavelength range 670–705 nm is included in figure 3 to highlight the expanded view of the first derivative of a Gaussian lineshape fit to accurately determine the characteristic wavelength of feature A to be 688 ± 0.9 nm ($E_A = 1.802 \pm 0.002$ eV) with a broadening parameter of 9.9 ± 0.4 nm ($\Gamma = 0.026 \pm 0.001$ eV). Peak A corresponds to the direct gap of $Ga_{1-x}Al_xAs$ barriers. The Al composition x is determined to be 0.26. This value is slightly lower than the intended value of 0.30. The appearance of an angle-independent feature labelled as B at around 816 nm for all DSPV spectra is noted. A plausible origin of this feature may be inferred by the nature of the angle dependence of the CM as discussed later. For the incident angle θ larger than 45°, a tiny feature located at the longer wavelength region corresponds to the onset of absorption of 1C–1H in the GaAs QWs. The inset of figure 3 shows the DSPV spectrum in the range of 840–850 nm for $\theta = 60°$. Shown by the open circles is the derivative of a Gaussian line shape fit, which is appropriate for excitonic transition [24]. The obtained value for the 1C–1H transition characteristic wavelength is 844.7 ± 1.2 nm ($E_{QW} = 1.468 \pm 0.002$ eV) with the broadening parameter 2.3 ± 0.5 nm ($\Gamma = 0.004 \pm 0.001$ eV) and denoted as C shown at the bottom of figure 3 by an arrow. Feature C corresponds well to the calculated 1C–1H transition of the QWs in the active region based on an envelope calculation [25] including

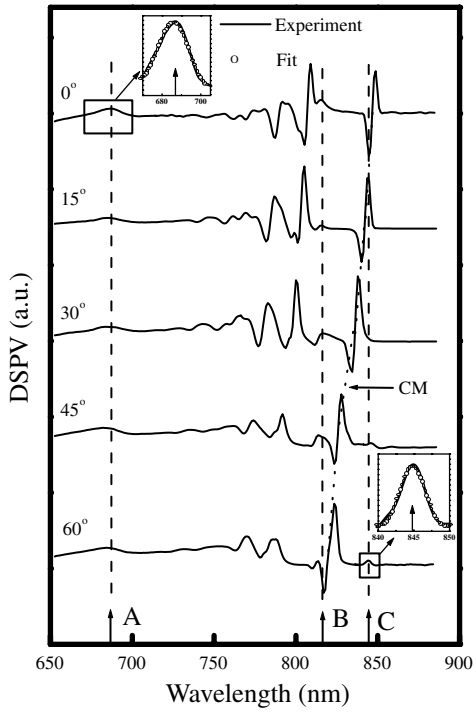

Figure 3. Room temperature DSPV spectra for different angles of incidence θ of the light beam. The spectra are shifted vertically for clarity. The angles of incidence are indicated on the left. With increasing θ the CM and other DBR features shift to shorter wavelength. The dotted line provides a guide to the eye for the angular dependence of the CM. DSPV features denoted by dashed lines that do not shift with θ are due to the interband transition of the GaAlAs barriers, CM at $\theta = 90°$ and the fundamental transition. The insets show the DSPV spectra in the range 670–705 nm for feature A at incident angle $\theta = 0°$ and 840–850 nm for feature C at incident angle $\theta = 60°$. The open circle curves are the first derivatives of a Gaussian lineshape fit for the GaAlAs interband transition and the 1C–1H excitonic transition denoted by arrows.

exciton binding energy and quantum confined Stark effect [26], using values of the conduction band offset $Q_c = 0.65$ and Al composition $x = 0.26$ deduced from feature A.

By increasing the incident angle θ the structures manifest themselves as due to the top DBR mirror features shifting to shorter wavelength. The highest lying feature at $\theta = 0°$ corresponds to the CM moving to shorter wavelength according to equation (1). Thus, while under normal incidence the CM almost coincides with the onset of the absorption of 1C–1H transitions of QWs, under light of oblique incidence it shifts toward shorter wavelength. At $\theta = 60°$ the CM has shifted by 26.8 nm and is well below the 1C–1H transition of QWs. It is interesting to note that the CM will shift monotonically downward and toward feature B with further increases of incident angle. In fact, at $\theta \sim 90°$ the CM feature merges with feature B. The angular behaviour of CM feature implies that feature B may just be corresponding to CM at 90° incidence. A relatively straightforward event of total internal reflection may account for the occurrence of feature B. The light multiply reflected by the DBR stacks must also be refracted by the layered active region to the extent that some of the light rays are bent so that the light ray paths are essentially parallel to the DBR stacks [5]. The enhanced sensitivity of the DSPS measurement enables the detection of signals resulting from total internal refection within the active region.

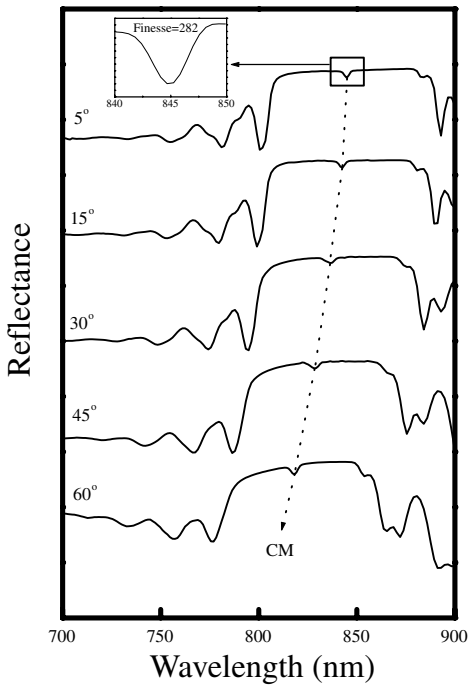

Figure 4. Reflectivity spectra at room temperature of the VCSEL structure for difference angles of incidence of the probe light. The inset shows the FP CM with higher spectral resolution. The dotted line, a guide to the eye, with an arrow indicates the CM moving steadily from long to short wavelengths with an increasing angle of incidence.

The room temperature angle-dependent R spectra are shown in figure 4. The R curve for $\theta = 5°$ shows a reflectivity plateau and a small dip due to the resonance mode of the FP cavity appearing at 845.8 nm. The quality of the cavity is attested by the measured finesse, $F = \lambda_{cav}/\text{FWHM} = 282$, where FWHM is the full width at half maximum [27]. Shown in figure 4 the dotted line, a guide to the eye, with an arrow indicates that the CM dip feature in the R spectra moves to shorter wavelength with increase angle of incidence.

Figure 5 summarizes the results of the angle-dependent SPS, DSPS and R measurements. The open triangles and closed circles are $\lambda_{QW}(\theta)$ determined from SPS and DSPS, respectively, while the closed triangles, open circles and open squares are $\lambda_{cav}(\theta)$ determined from SPS, DSPS and R, respectively. The angle-independent nature of λ_{QW} is quite clear from SPV and DSPV spectra as illustrated in figure 5. The values for λ_{cav} determined from SPS, DSPS and R spectra agree well with each other. The dependence of λ_{cav} on θ is fitted with equation (1) to deduce the effective cavity length and effective refraction index to be 2384 ± 20 Å and 3.542 ± 0.002, respectively. The value of the determined effective cavity length is in a reasonable agreement with the intended number of 2480 Å.

4.3. Temperature-dependent experiments at fixed angle of incidence

Figures 6(a) and (b) show representative SPV spectra recorded at $\theta = 0°$ and 60°, respectively, with temperature increasing from 25 to 215 °C. The feature due to the QW transition is seen to red shift with increasing temperature. The CM also shows a red shift, due to thermal expansion of the cavity and a change in index of refraction n, but at a much slower pace. The dashed line

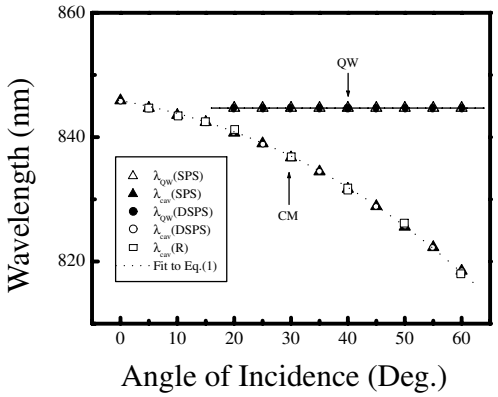

Figure 5. Angle dependence of the fundamental excitonic QW transition and CM wavelengths determined from the SPS, DSPS and R measurements. The open triangles and closed circles are $\lambda_{QW}(\theta)$ determined from SPS and DSPS, respectively, while the closed triangles, open circles and open squares are $\lambda_{cav}(\theta)$ determined from SPS, DSPS and R, respectively. The dotted line is a least-squares fit to equation (1).

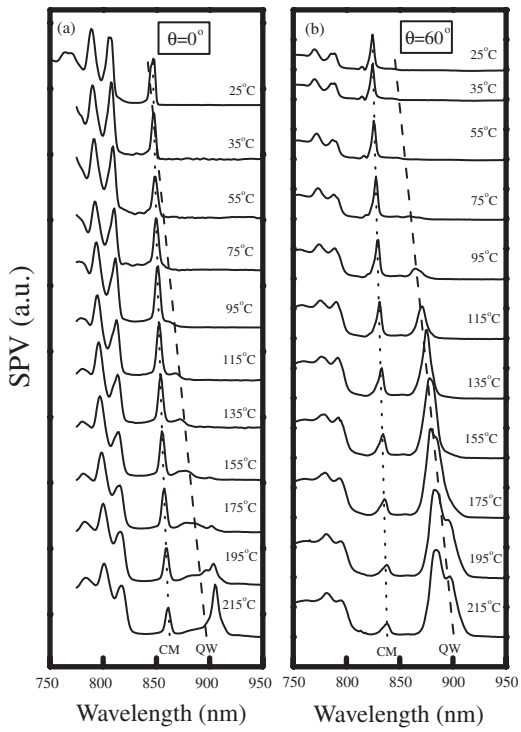

Figure 6. Results of temperature variation (25 °C $\leqslant T \leqslant$ 215 °C) experiments on SPS measurements at (a) $\theta = 0°$ and (b) $\theta = 60°$. The dotted and the dashed lines are guides to the eye, of $\lambda_{cav}(T)$ and $\lambda_{QW}(T)$ respectively. $\lambda_{QW}(T)$ shifts to longer wavelength with increasing temperature, while $\lambda_{cav}(T)$ also shows a red shift but at a much slower pace.

and dotted line, guides to the eye, show the temperature dependence of the QW transition and CM respectively. Figure 7 summarizes the results of the temperature-dependent SPS, DSPS

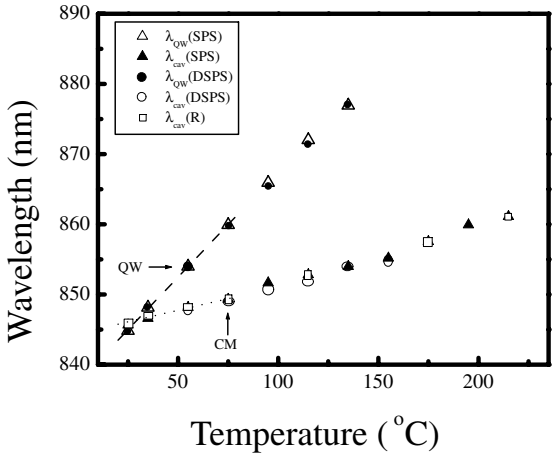

Figure 7. Temperature dependence of the fundamental excitonic QW transition and CM wavelengths determined from the SPS, DSPS and *R* measurements. The open and closed triangles are $\lambda_{QW}(T)$ and $\lambda_{cav}(T)$, respectively, as determined from SPS. The closed and open circles are $\lambda_{QW}(T)$ and $\lambda_{cav}(T)$, respectively, as determined from DSPS, while the open squares are $\lambda_{cav}(T)$ as determined from NIR. The dashed and dotted lines are least-squares fits to a linear expression for $\lambda_{QW}(T)$ and $\lambda_{cav}(T)$, respectively, in the range of 25–75 °C.

and *R* measurements. The open and closed triangles in figure 7 are $\lambda_{QW}(T)$ and $\lambda_{cav}(T)$, respectively, from SPS investigation. The closed and open circles in figure 7 are $\lambda_{QW}(T)$ and $\lambda_{cav}(T)$, respectively, as determined from DSPS. The open squares in figure 7 are $\lambda_{cav}(T)$ from NIR. There is good agreement among the SPS and DSPS data and the relevant *R* measurements. The experimental data were then fitted with equation (3) to obtain two different linear functions of temperature for the two wavelengths of interest as $\lambda_{cav}(T) = 845.8 + 0.08(T - 25)$ nm (the dotted lines) and $\lambda_{QW}(T) = 844.7 + 0.25(T - 25)$ nm (the dashed lines), where T is in °C. The variation of λ_{QW} is about three times faster than λ_{cav}, as T is increased. The obtained $\lambda_{QW}(T)$ extrapolates well to the angle-dependent results at room temperature ($T = 25$ °C). The two lines cross at $T \sim 31$ °C when the onset of QW/CM resonance is taking place.

4.4. Superior features of SPS and DSPS over other techniques for characterizing VCSEL structures

The DSPS and SPS have a number of advantages over other methods such as *R*, PR and PC. The SPS and DSPS are both related to the photovoltaic effect, which is very sensitive to the low light levels that reach the QW region through the top DBR mirrors. The wavelength-modulated DSPS yields a derivative spectrum, which can further improve the accuracy and sensitivity of the SPS dramatically. The DSPV spectrum can be fitted by a lineshape function and the wavelengths (energies) of various transitions may be evaluated to within a few ångstroms (meV) at room temperature. While both the CM and 1C–1H transition are always observed in DSPS and SPS, for PR in some cases only the latter is observed. In DSPS and SPS, a rich interference pattern related to the properties of the DBR is observed in contrast to PR. In addition, DSPS has an advantage over PR in that it requires no pumping beam. The techniques of SPS, DSPS and PR are contactless and require no special mounting of the sample, and hence are completely nondestructive and can be employed on the entire wafer. This attribute is superior to PC and differential photocurrent spectroscopy where contact must be made with the sample and hence some degree of damage to the sample is inevitable.

5. Summary

In summary we have performed an angle- and temperature-dependent SPS and DSPS investigation of a GaAs/GaAlAs VCSEL structure. At a fixed temperature, the CM and DBR mirror features show a blue shift with increasing incident angle θ, while the QW transition remains unchanged. The wavelengths of the QW transition and CM may be evaluated accurately through the line shape fit to the DSPV spectrum. At fixed θ, λ_{QW} shows a red shift with increasing temperature, while λ_{cav} also increases but at a much slower pace than λ_{QW}. The results demonstrate that the characterization of VCSEL wafers by angle- and temperature-dependent DSPS/SPS allow one to obtain detailed information about excitonic transitions and cavity properties, and hence to assess the overlap between the gain spectrum of the active QW region and the CM in a VCSEL structure. This study demonstrates the considerable potential of SPS for the characterization of the VCSEL structures.

Acknowledgments

The authors J S Liang, S D Wang and Y S Huang acknowledge the support of the National Science Council of the Republic of China under Project No NSC90-2215-E-011-006. One of the authors (FHP) was supported by Army Research Laboratory contract No DAAD17-99-C-0072 and the New York State Science and Technology Foundation through its Centers for Advanced Technology programme.

References

[1] Dutta N K, Nichols D T, Avkshoori D, Sivco D L and Cho A Y 1995 *Appl. Phys. Lett.* **67** 588
[2] Banwell T C, Von Lehmen A C and Cordell R R 1993 *IEEE J. Quantum Electron.* **29** 635
[3] Iga K and Koyama F 1993 *Surface Emitting Semiconductor Lasers and Arrays* ed G A Evans and J M Hammer (San Diego, CA: Academic) p 71
[4] Soda H, Iga K, Kitahara C and Suematsu Y 1979 *Japan. J. Appl. Phys.* **18** 2329
[5] Gramlich S, Sebastian J, Weyers M and Hey R 1995 *Phys. Status Solidi* a **152** 293
[6] Moneger S, Qiang H, Pollak F H, Mathine D L, Droopad R and Maracas G 1996 *Solid-State Electron.* **39** 871
[7] Berger P D, Bru C, Benyattou T, Guillot G, Chenevas-Paule A, Couterier L and Grosse P 1996 *Appl. Phys. Lett.* **68** 4
[8] Klar P J, Rowland G, Sale T E, Hosea T J C and Grey R 1998 *Phys. Status Solidi* a **170** 145
[9] Klar P J, Rowland G, Thomas P J S, Onischenko A, Sale T E, Hosea T J C and Grey R 1999 *Phys. Rev.* B **59** 2894
[10] Klar P J, Rowland G, Thomas P J S, Onischenko A, Sale T E, Hosea T J C and Grey R 1999 *Phys. Rev.* B **59** 2902
[11] Vicente P M A, Thomas P J S, Lancefield D, Sale T E, Hosea T J C, Adams A R, Klar P J and Raymond A 1999 *Phys. Status Solidi* b **211** 255
[12] Sale T E, Hosea T J C and Thomas P J S 2000 *IEEE. Photon. Technol. Lett.* **12** 1328
[13] Choulis S A, Ghosh S and Hosea T J C 2000 *J. Appl. Phys.* **88** 5547
[14] Ghosh S, Hosea T J C and Constant S B 2001 *Appl. Phys. Lett.* **78** 3250
[15] Jaeger A, Petroff P M and Lowes T D 2001 *Appl. Phys. Lett.* **78** 3012
[16] Huang Y S, Malikova L, Pollak F H, Shen H, Pamulapati J and Newman P 2000 *Appl. Phys. Lett.* **77** 37
[17] Liang J S, Huang Y S, Tien C W, Chang Y M, Chen C W, Li N Y, Li P W and Pollak F H 2001 *Appl. Phys. Lett.* **79** 3227
[18] Liang J S, Wang S D, Huang Y S, Tien C W, Chang Y M, Chen C W, Li N Y, Lin D Y and Pollak F H 2002 *Appl. Phys. Lett.* **80** 752
[19] Huang Y S, Malikova L, Pollak F H, Debray J P, Hoffman R, Amtout A and Stall R A 2002 *J. Appl. Phys.* **91** 6203
[20] Balestra C L, Lagowski J and Gatos H C 1971 *Surf. Sci.* **26** 317
[21] Lagowski J 1994 *Surf. Sci.* **299/300** 92
[22] Tabatabaei S A, Iliadis A A and Wood C E C 1995 *J. Electron. Mater.* **24** 87

[23] Aigouy L, Pollak F H, Petruzzello J and Shahzad K 1997 *Solid State Commun.* **102** 877
[24] Pollak F H and Shen H 1993 *Mater. Sci. Eng.* R **10** 275
[25] Bastard G 1986 *IEEE J. Quantum Electron.* **22** 1625
[26] Singh J 1993 *Physics of Semiconductors and Their Heterostructures* (New York: McGraw-Hill)
[27] Yeh P 1991 *Optical Wave in Layered Media* (Singapore: Wiley) p 149